Electronic Supplementary Material (ESI) for Chemical Communications.
This journal is © The Royal Society of Chemistry 2020

Electronic Supplementary Information

Organic Single Crystals of Cyano-Substituted p-Phenylene Vinylene Derivatives as Transistors with Low Surface Trap Density

Jian Deng, Yuejuan Wan, Chang Cai, Cheng Gu and Yuguang Ma

State Key Laboratory of Luminescent Materials and Devices, Institute of Polymer Optoelectronic Materials and Devices, South China University of Technology, No. 381 Wushan Road, Tianhe District, Guangzhou 510640, P. R. China

Contents

Experimental section

Materials.

2,2'-(1,4-phenylene)diacetonitrile, thiophene-3-carbaldehyde, benzo[1,2-b:5,4-b']dithiophene, Benzo[1,2-b:5,4-b']dithiophene-2,6-dicarbaldehyde, 2-phenylacetonitrile, tert-butyl alcohol, tetrabutylammonium hydroxide, potassium tert-butoxide, dichloromethane, *n*-BuLi, *N*,*N*-dimethylformamide (DMF), tetrahydrofuran (THF), H_2O_2, H_2SO_4, acetone, and ethanol were purchased from *J&K* Chemicals. DMSO-d_6, $CDCl_3$, petroleum ether, chloroform, and chlorobenzene were purchased from TCI. CYTOP was purchased from ACG Cop.. All the chemicals were used directly without further purification.

N_2 (99.9999%) and Ar (99.9999%) were purchased form Mulai gas company.

Synthesis of materials

Synthesis of (2Z,2'Z)-2,2'-(1,4-phenylene)bis(3-(thiophen-3-yl)acrylonitrile) (α-PBTA): The α-PBTA was synthesized by Knoevenagel reaction. Thiophene-3-carbaldehyde (224 mg, 2 mmol), 2,2'-(1,4-phenylene)diacetonitrile (156.2 mg, 1 mmol), tert-butyl alcohol (t-BuOH, 10 mL), and THF (5 mL) were placed in a two-neck flask whose inner gas was replaced by N_2. The mixture was stirred at 46 °C for 30 min. Then tetrabutylammonium hydroxide (TBAH, 51.9 mg, 0.2 mmol) and potassium tert-butoxide (t-BuOK, 22.4 mg, 0.2 mmol) were dissolved in 3 mL THF and were added into the system. The mixture was stirred at 46 °C under N_2 for another 30 min. After cooling down to room temperature, the reaction mixture was filtered. The precipitates were purified by column chromatography (dichloromethane as the eluent), and then dried in vacuum at 80 °C to give α-PBTA as a blue-green solid in 68% isolated yield. ^{1}H NMR (500 MHz, DMSO-d_6): δ (ppm) = 8.27 (1H, d, J = 2.1 Hz), 8.20 (1H, s), 7.87 (2H, s), 7.85 (1H, d, J = 5.3 Hz), 7.79 (1H, dd, J = 5.1, 3.0 Hz). Because of poor solubility of α-PBTA, its ^{13}C NMR signals were not detected. APCI MS: calcd. for $[M]^+$, m/z = 344.04; found m/z = 344.0. Elemental analysis: calcd. for $C_{20}H_{12}N_2S_2$: C, 69.74; H, 3.51; N, 8.13; S, 18.62; found: C, 69.78; H, 3.33; N, 8.04; S, 18.85.

Synthesis of benzo[1,2-b:5,4-b']dithiophene-2,6-dicarbaldehyde: Under argon atmosphere, benzo[1,2-b:5,4-b']dithiophene (570.9 mg, 3.0 mmol) was added into a dry flask charged with dry

THF (20 mL) at -78 °C. Then *n*-BuLi (2.5 M in hexane, 5.0 mL, 4.0 mmol) was added dropwise at -78 °C. After stirred for 3 h, DMF (1.2 mL, 15 mmol) was added dropwise and stirred for another 2 h. The reaction mixture was warmed to 25 °C and stirred for 12 h, then quenched by adding deionized water (5.0 mL). The organic phase was extracted with acetic ether for three times and concentrated. The crude residue was purified by column chromatography with a mixture of dichloromethane and petroleum ether (v/v = 3:2) as eluent. The solution of product was dried with $MgSO_4$ and was evaporated in vacuum to give light yellow powder with isolated yield of 54%. ^{1}H NMR (500 MHz, $CDCl_3$): δ (ppm) = 10.09 (2H, s), 8.49 (1H, s), 8.36 (1H, s), 8.08 (2H, s). ^{13}C NMR (126 MHz, DMSO-d_6): δ (ppm) = 186.97, 143.74, 141.70, 137.53, 136.73, 125.58, 118.35. APCI MS: calcd. for $[M]^+$, m/z = 246.30; found m/z = 246.0. Elemental analysis: calcd. for $C_{12}H_6O_2S_2$: C, 58.52; H, 2.46; S, 26.03; found: C, 58.34; H, 2.66; S, 25.91.

Synthesis of (2Z,2'Z)-3,3'-(benzo[1,2-b:5,4-b']dithiophene-2,6-diyl)bis(2-(thiophen-3-yl)acrylonitrile) (β-DBPA): Benzo[1,2-b:5,4-b']dithiophene-2,6-dicarbaldehyde (246 mg, 1 mmol), 2-phenylacetonitrile (234 mg, 2.0 mmol), THF (5 mL), and tert-butyl alcohol (t-BuOH, 20 mL) were placed in a two-neck flask whose inner gas was replaced by N_2. The mixture was stirred at 66 °C for 5 h. Then tetrabutylammonium hydroxide (TBAH, 51.9 mg, 0.2 mmol) and potassium tert-butoxide (t-BuOK, 22.4 mg, 0.2 mmol) were dissolved in 3 mL THF and were added into the system. The mixture was stirred at 66 °C under N_2 for another 30 min. Then the system was cooled down to room temperature, poured into the methanol solution with a drop of acetic acid. The yellow solid was obtained via filtration and dried under vacuum at 60 °C with an isolated yield of 50%. Because of poor solubility of β-DBPA, its ^{1}H and ^{13}C NMR signals were not detected. APCI MS: calcd. for $[M]^+$, m/z = 444.57; found m/z = 444.0. Elemental analysis: calcd. for $C_{28}H_{16}N_2S_2$: C, 75.65; H, 3.63; N, 6.30; S, 14.42; found: C, 75.63; H, 3.70; N, 6.27; S, 14.40. The purity, chemical structure and crystal structure were determined by single-crystal X-ray diffraction.

Preparation of the organic single crystals:

The growth procedure of the organic single crystals was executed in a quartz tube which was placed in the furnace. The furnace was designed with two separated heating sources, which ensured precise and respective control over their temperatures. During the growth of the crystals, the furnace was filled with flowing ultrapure argon. The optimal condition for the growth of the crystals were listed

in Supplementary Table S1). Under these conditions, plenty of lamellar crystals were hung inside the wall of the quartz tubes. All the obtained crystals were stored in the quartz tubes under nitrogen atmosphere in glove box.

General instrumental analysis:

^{1}H and ^{13}C NMR spectra were recorded on a Bruker AVANCE HD III 500M NMR spectrometer, where the chemical shifts (δ in ppm) were determined with respect to tetramethylsilane (TMS) as an internal reference. Mass spectrometry data of compounds were obtained on a Waters ACQUITY TQD liquid chromatograph-mass spectrometer using APCI ionization. Elemental analysis was performed on a Flash EA 1112, CHNS-O elemental analyser. TGA measurements were performed on a PerkinElmer Thermal analysis under N_2, by heating to 800 °C at a rate of 5 °C min^{-1}. DSC measurements were performed on a NETZSCH (DSC-204) unit at a heating rate of 10 °C min^{-1} under N_2.

Single-crystal X-ray diffraction (SXRD) data were recorded on an XtaLAB P200 FR-X using a VariMax Mo Optic with Mo−Kα radiation (λ = 0.71075 Å) or Cu−Kα (λ = 1.54184 Å). The structure was solved using direct methods and refined by full-matrix least-squares cycles in SHELX 2014/7[S1]. All non-hydrogen atoms were refined using anisotropic thermal parameters. The film thickness were measured on a Vecco DEKTAK 150 surface profiler. Cyclic voltammetry was recorded on a standard three-electrode electrochemical cell attached to a CHI 660C electrochemical workstation in acetonitrile/THF with 0.1 M $TBAPF_6$ as the supporting electrolyte at a scan rate of 50 mV s^{-1}. The potentials were measured against an Ag/Ag^{+} reference electrode with ferrocene as the internal standard.

Fourier transform Infrared (FT-IR) spectra were recorded on a VERTEX 80 V Fourier transform infrared spectrometer with KBr as reference. UV-Vis spectra were recorded on a Shimadzu UV-3600 spectrometer. Photoluminescence spectra were recorded on a Shimadzu RF-5301PC spectrophotometer. Photoluminescence quantum yields (PLQY) were measured on an Absolute PL Quantum Yield Spectrometer C113. Fluorescence images were recorded through Leica fluorescence microscope with DM4000 excitation from 340 to 380 nm.

Fabrication and characterization of the OFETs:

The highly conductive p-silicon wafers (electrical impedance rate of 0.002 ~ 0.005 Ω mm^{-1}) with 200 nm thermally grown SiO_2 layer were cut into 1 × 1 cm^2 wafers and etched the SiO_2 layer at the corner. The wafers were cleaned under ultrasonication by chloroform, acetone, and ethanol (twice for each solvent), respectively. Then the insulated surfaces of the silicon wafers were modified by ultra-high molecular weight polymethyl-methacrylate (PMMA) films. The PMMA particle were dissolved in chlorobenzene (20 mg mL^{-1}). The silicon wafers were heated to 80 °C, and then the PMMA solution was spin coated onto the wafers with the rotation rate of 2000 rpm. The wafers were annealed on a hot stage at 180 °C for 90 s to remove the solvents in the films. The film thickness of PMMA was 80 nm. The CYTOP was spin coated with similar method. The concentration of CYTOP were 20 wt%, and the resulted wafers were annealed on a hot stage at 100 °C for 24 h to remove the solvent. The film thickness of CYTOP was 80 nm.

The organic crystals after careful selection were tightly pasted to the surface of the PMMA or CYTOP-modified silicon wafers with the assistance of the electrostatic interaction. Then the substrates and the crystals were covered with the shadow masks with two-square shape, and were transferred into deposition chamber. Before depositing the electrodes, the chamber was evacuated to 1 × 10^{-4} Pa. The gold electrodes were deposited with the rate of 0.3 nm s^{-1}. When fabricating the OFETs with calcium/gold asymmetric electrodes, the multilayer calcium and gold electrodes were deposited onto the crystals with the rates of 0.6 and 0.3 nm s^{-1}, respectively. The asymmetric electrodes configuration was realized by the shadow mask with one hole and independent evaporate of metals. The thicknesses of the calcium and gold were 150 and 200 nm, respectively. During the entire deposition progress, the pressure of the chamber was kept below 1 × 10^{-4} Pa.

The characterization of the electrical properties of the devices was performed by the semiconductor parameter analyzer (Agilent Technologies B1500A and Keithley 2636B) in the glove box, in which the concentrations of the oxygen and water vapor were kept below 0.1 ppm, respectively.

For the OFETs with symmetric electrodes, the lengths of the channel were 20 ~ 200 μm, corresponding to the sizes of shadow masks. For the OFETs with asymmetric electrodes, the lengths of the channel were 10 ~ 400 μm, depending on the fabrication conditions. The gate-channel capacitance per unit area (C_i) was calculated to be 1.20 × 10^{-8} F cm^{-2} based on the thickness of SiO_2 and PMMA layers, and 9.71× 10^{-9} F cm^{-2} based on the thickness of SiO_2 and CYTOP layers. The photographs of the OLETs were recorded by the Keyence microscope VHX-900F with the long

work distance lens (VH-Z50L), whose focal length was fixed to 8 cm. The channel length and width ratio were calculated with the captured photographs by GIMP 2.10.

Calculation of subthreshold swing and trap density

The subthreshold swing (S) was extracted using equation S1.

$$S = \frac{dV_g}{d\lg(I_d)} \tag{S1}$$

The density of the interface trap states (N_t) at the semiconductors and dielectric interface was calculated using equation S2[S1].

$$N_t = \left[S\lg(e)/(kT/q) - 1\right]C_i/q \tag{S2}$$

Where,

e: Euler's number,

C_i: gate dielectric capacitance,

k: Boltzmann's constant,

T: absolute temperature,

q: electronic charge.

There was another way to extract the total trap density ($N_t^{'}$) with the threshold voltage above tun-on voltage (V_{tto}) with equation S3[S2].

$$N_t^{'} = C_i\left|V_{tto}\right|/q = C_i\left|V_{th} - V_{on}\right|/q \tag{S3}$$

Where,

V_{on}: turn on gate voltage.

As a comparing, N_t and $N_t^{'}$ were respectively calculated and listed in Table S4.

Calculation of defects in organic crystals

Defects in organic crystals were extracted from the interfacial traps and lattice parameters. Here, we assumed the carrier migration in the ab-plane of crystal. The area of the unit cell in ab-plane was calculated by length of unit cell, a and b, as well as angle γ between a and b (equation S4).

$$A = \left|a\right|\left|b\right|\sin\gamma \tag{S4}$$

With the above area of unit cell, we could know how many cells was in unit area. The trap density demonstrated the upper limit of defects in organic crystal surface. If we assumed the carrier migrated in single molecular layer, the defects density was extracted by equation S5.

$$D = \frac{N_t}{AZ^*} \quad \text{(S5)}$$

where,

D, defects density (upper limit) in crystal surface. Its reciprocal meant no more than 1 defect existed in so many molecules of crystal surface.

Z*, the molecule number in ab-plane of single unit cell.

Supplementary Figures

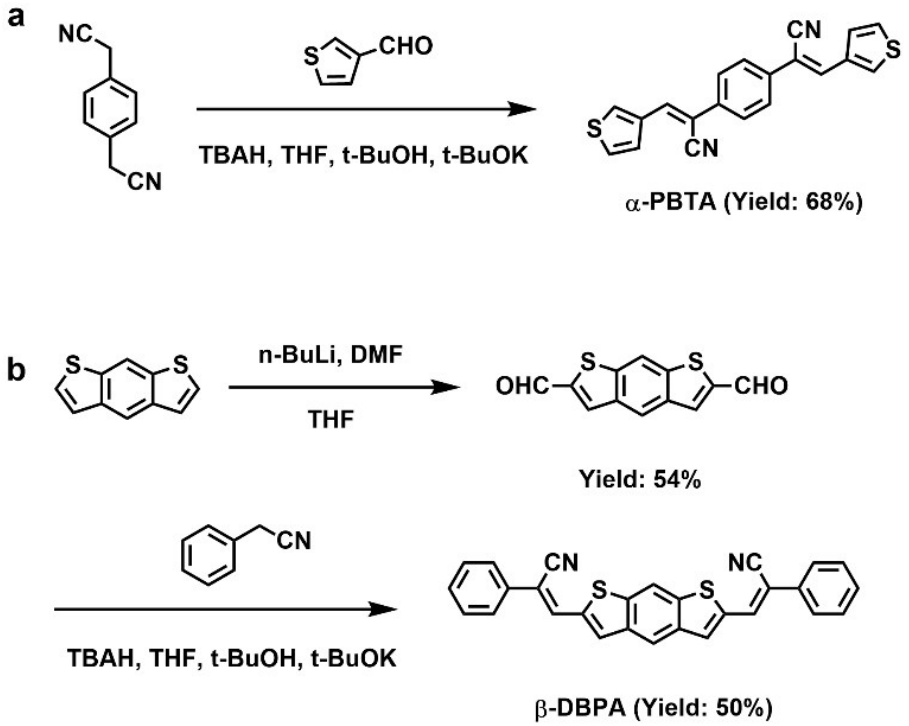

Figure S1. Synthesise of (a) α-PBTA and (b) β-DBPA.

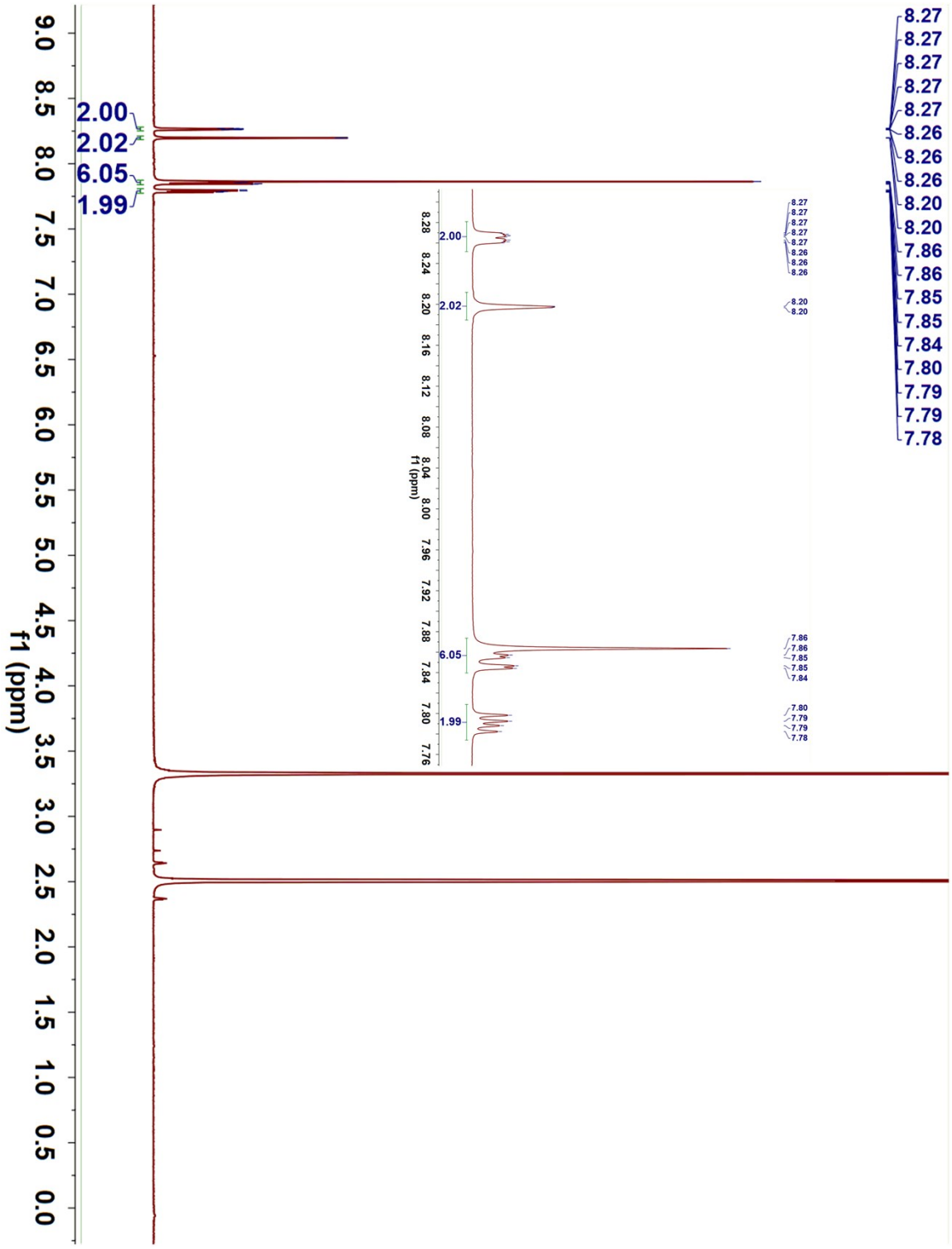

Figure S2 ^{1}H NMR spectra of α-PBTA.

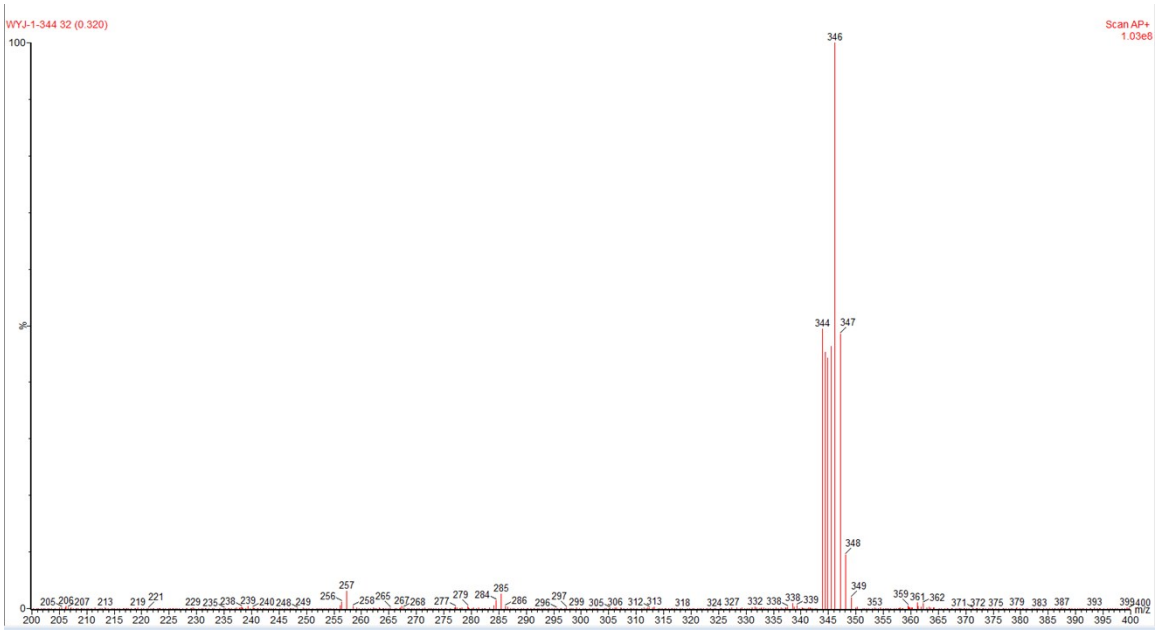

Figure S3 APCI mass spectra of α-PBTA.

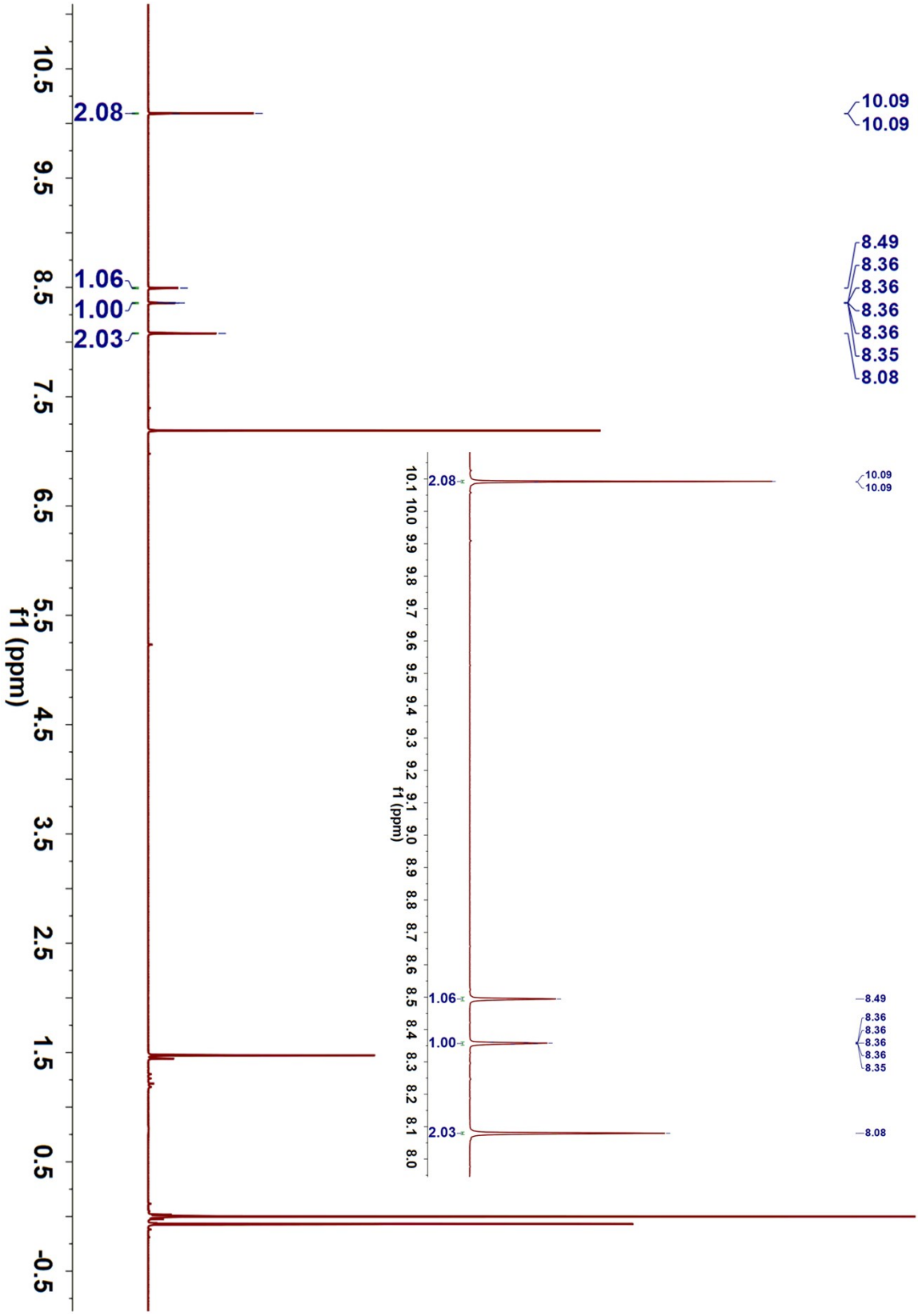

Figure S4 ^{1}H NMR spectra of benzo[1,2-b:5,4-b']dithiophene-2,6-dicarbaldehyde.

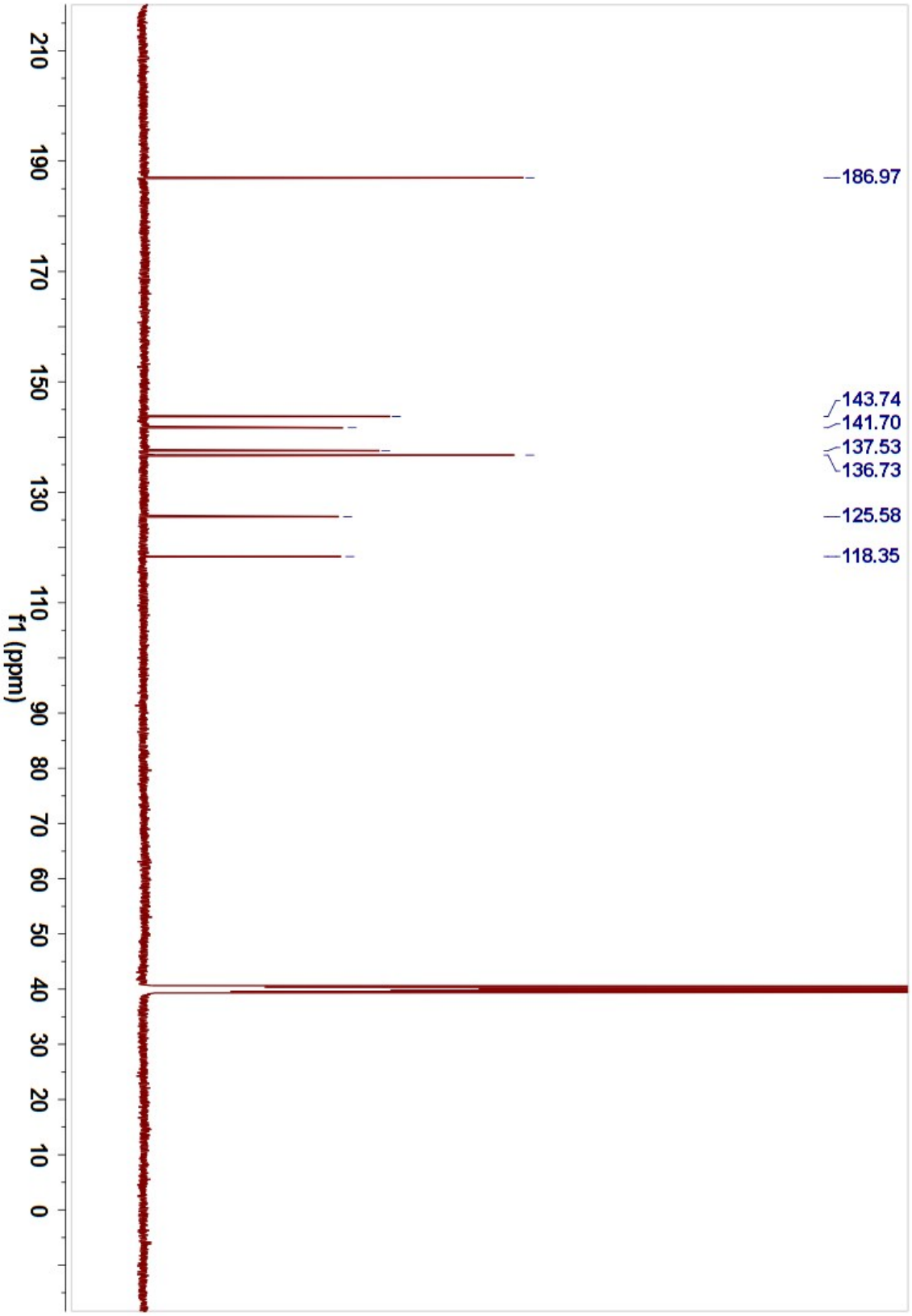

Figure S5 ^{13}C NMR spectra of benzo[1,2-b:5,4-b']dithiophene-2,6-dicarbaldehyde.

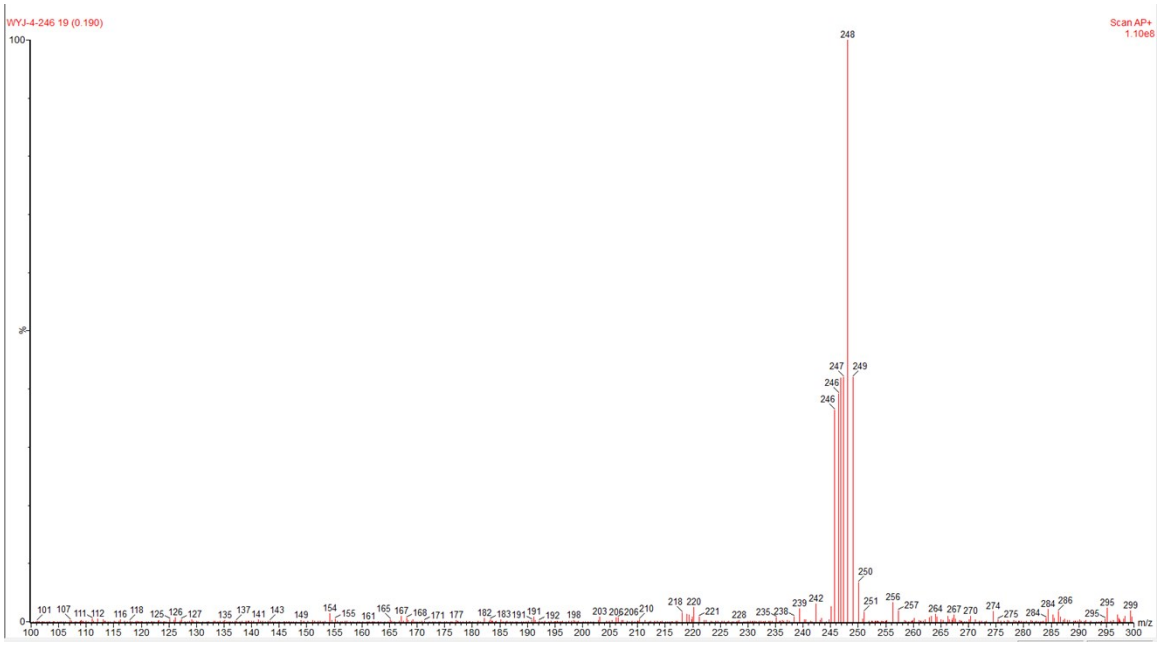

Figure S6 APCI mass spectra of benzo[1,2-b:5,4-b']dithiophene-2,6-dicarbaldehyde.

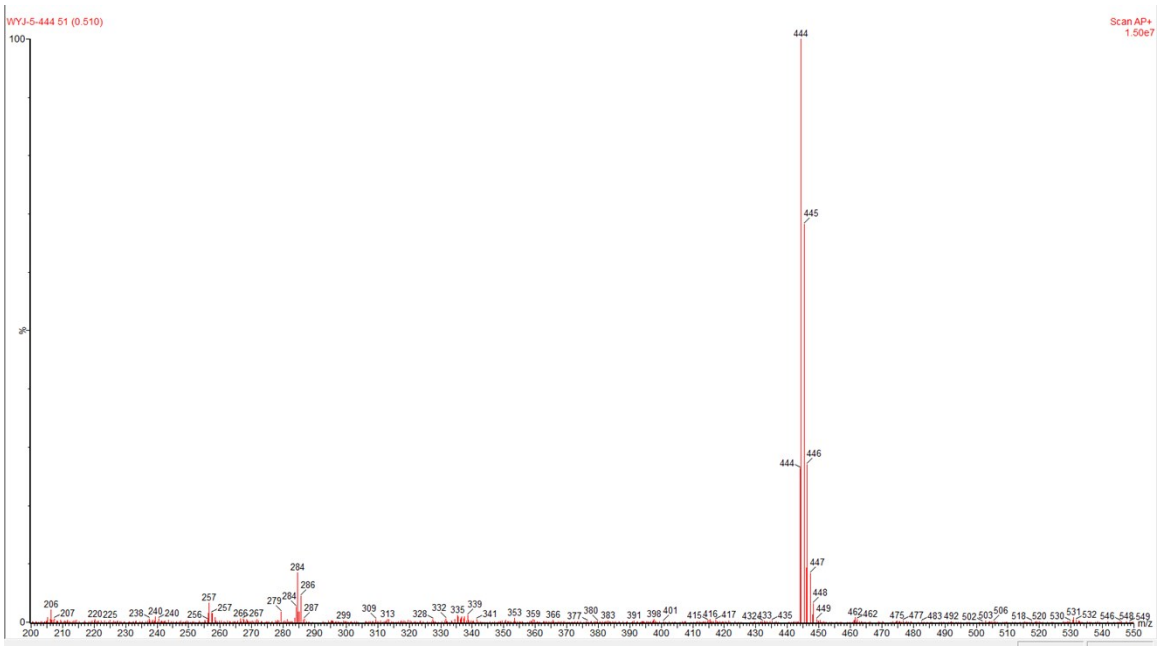

Figure S7 APCI mass spectra of β-DBPA.

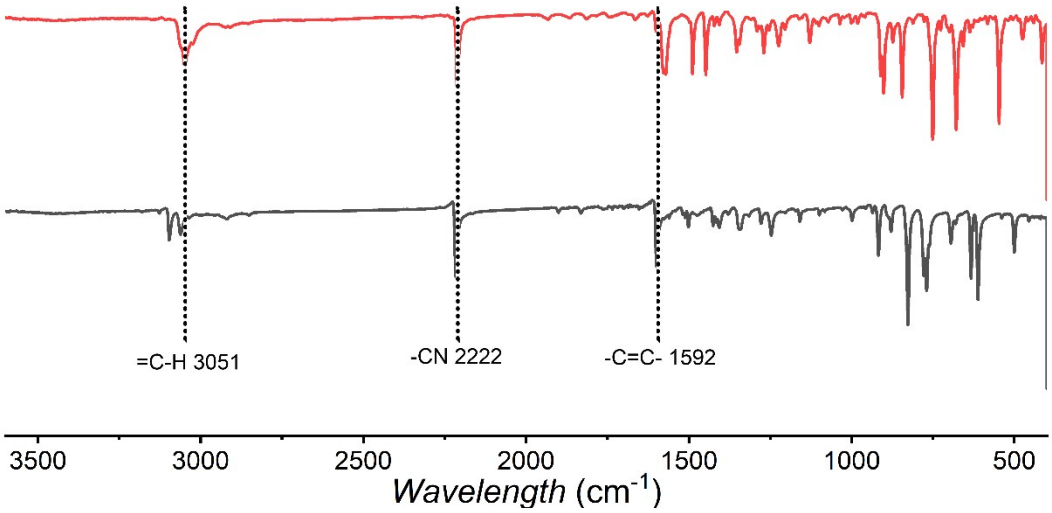

Figure S8 FT-IR spectra of (black) α-PBTA and (red) β-DBPA. The IR spectra exhibited a significant stretching vibration band at 2222 cm^{-1}, which was assigned to the vibration of C≡N bonds.

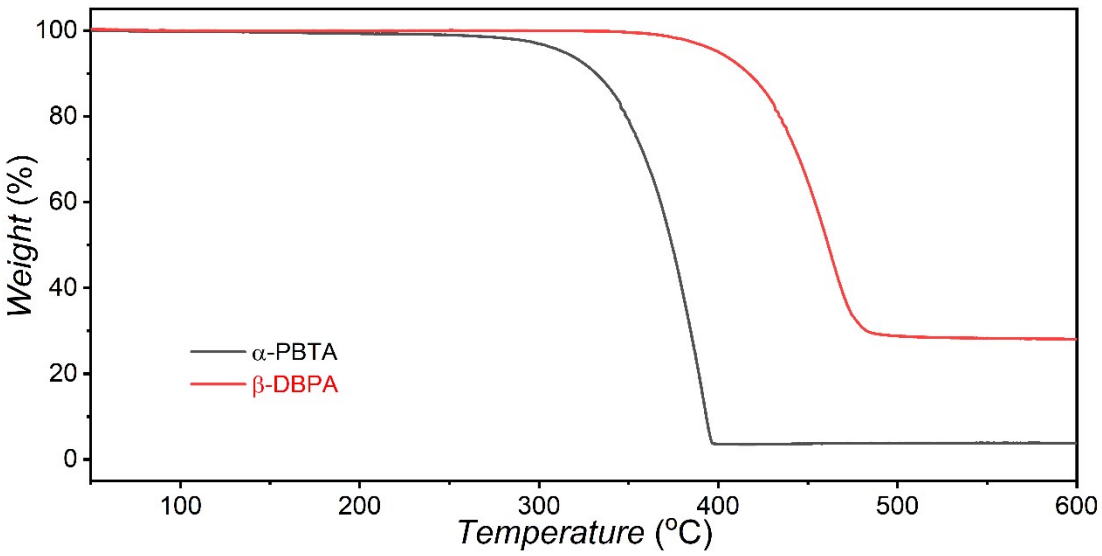

Figure S9 TGA of α-PBTA and β-DBPA, revealing the decomposition temperatures of 314 and 400 ºC, respectively.

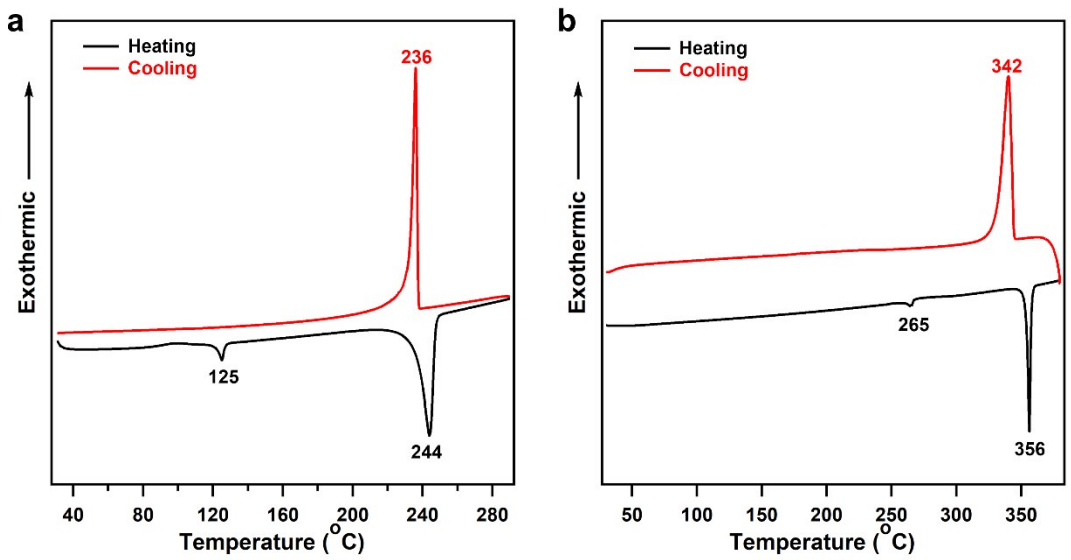

Figure S10 DSC of (a) α-PBTA and (b) β-DBPA.

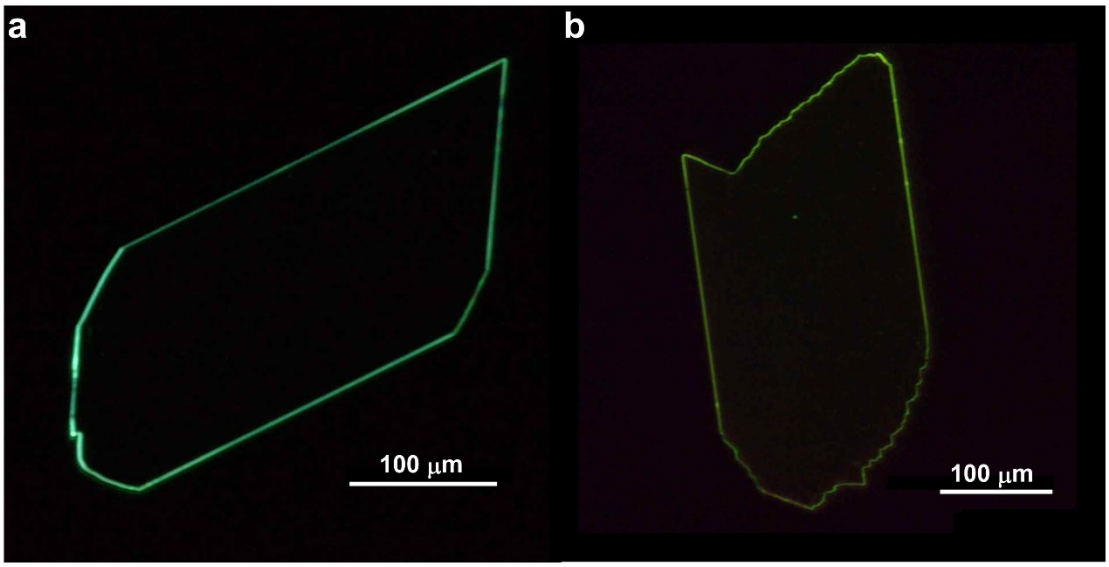

Figure S11 Crystals of (a) α-PBTA and (b) β-DBPA under UV irradiation.

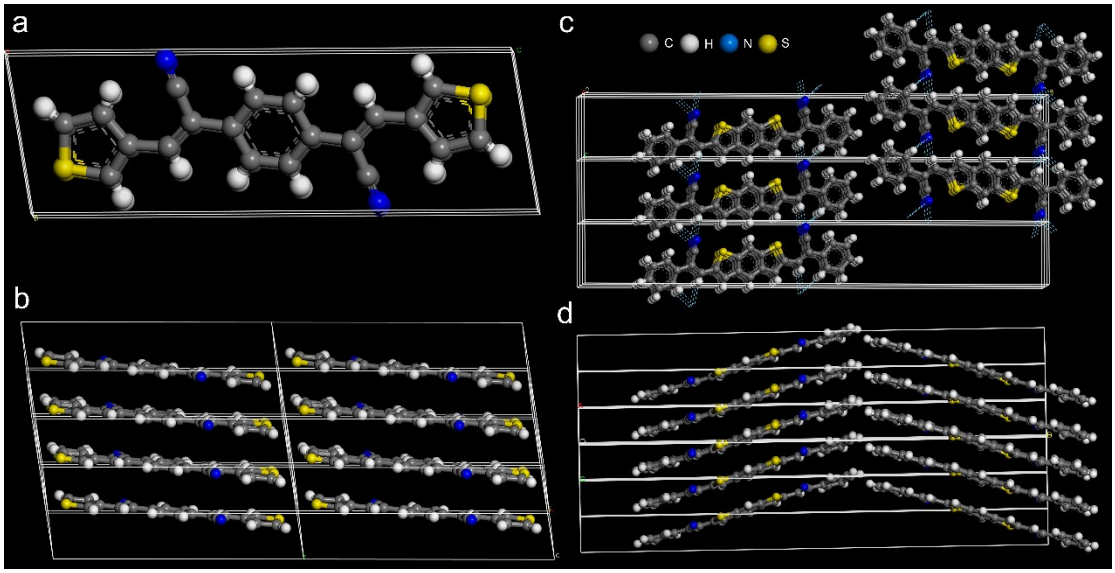

Figure S12 (a) Single-crystal structure of the α-PBTA crystals. (b) uniaxially orientated stacking in the lamellar crystal of α-PBTA. (c) Single-crystal structure of the β-DBPA crystals, revealing the multiple hydrogen bonds (sky-blue dashed lines). (d) herringbone stacking in the lamellar crystal of β-DBPA.

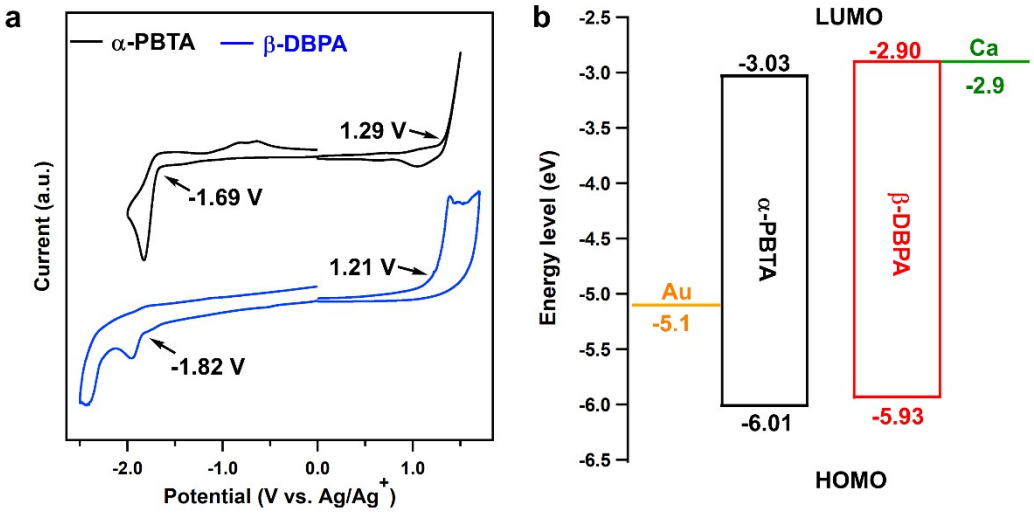

Figure S13 (a) Cyclic voltammetry (CV) of the α-PBTA and β-DBPA crystals, showing the onset oxidative and reductive potentials. (b) Energy diagram of the organic crystal OFETs. The HOMO and LUMO energy levels were calculated from the onset oxidative and reductive potentials in the CV profiles.

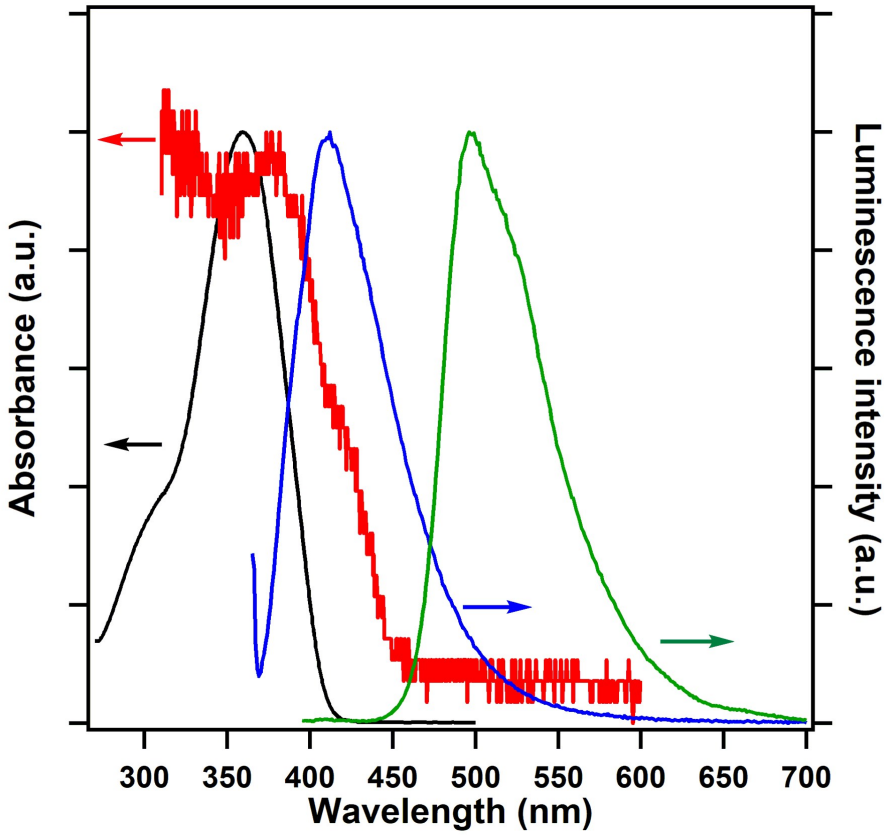

Figure S14 Absorption and fluorescence spectra of α-PBTA in solution state and in crystal state. Black curve: UV in THF solution; red curve: UV in 2DOSCs; blue curve: PL in THF solution; green curve: PL in 2DOSCs.

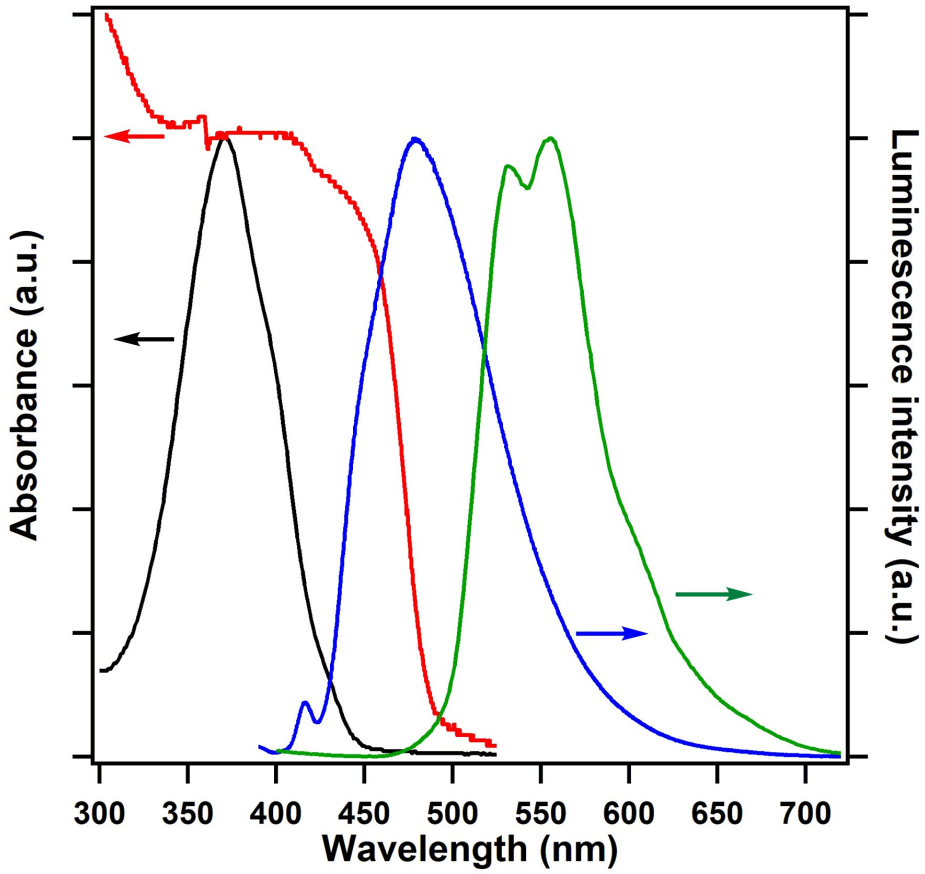

Figure S15 Absorption and fluorescence spectra of β-DBPA in solution state and in crystal state. Black curve: UV in THF solution; red curve: UV in 2DOSCs; blue curve: PL in THF solution; green curve: PL in 2DOSCs.

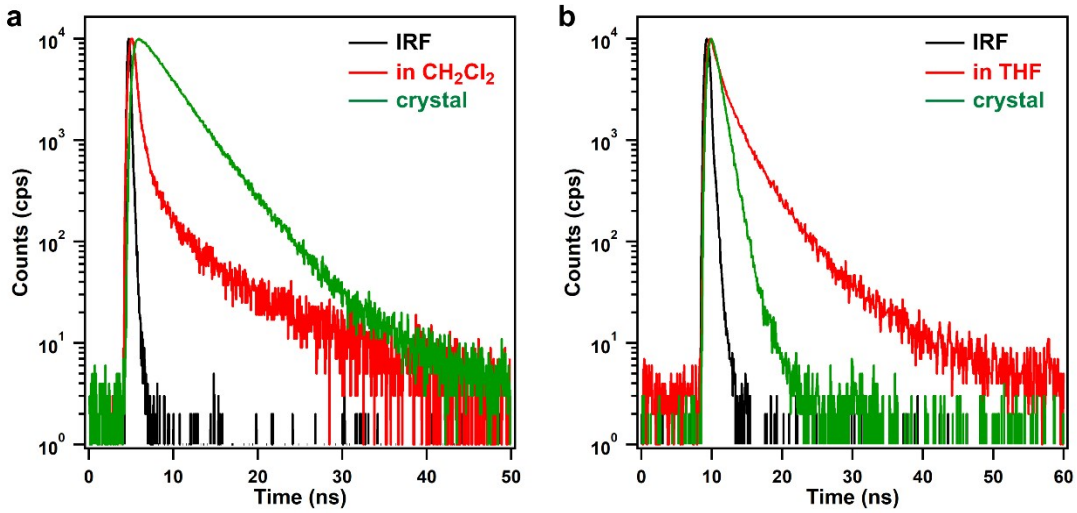

Figure S16 (A) Fluorescence decay profiles of the α-PBTA in dilute CH_2Cl_2 solution (1×10^{-5} mol L^{-1}) and 2DOSCs. The black curve was the IRF of the instruments. (B) Fluorescence decay profiles of the β-DBPA in dilute THF solution and 2DOSCs. The black curve was the IRF of the instruments.

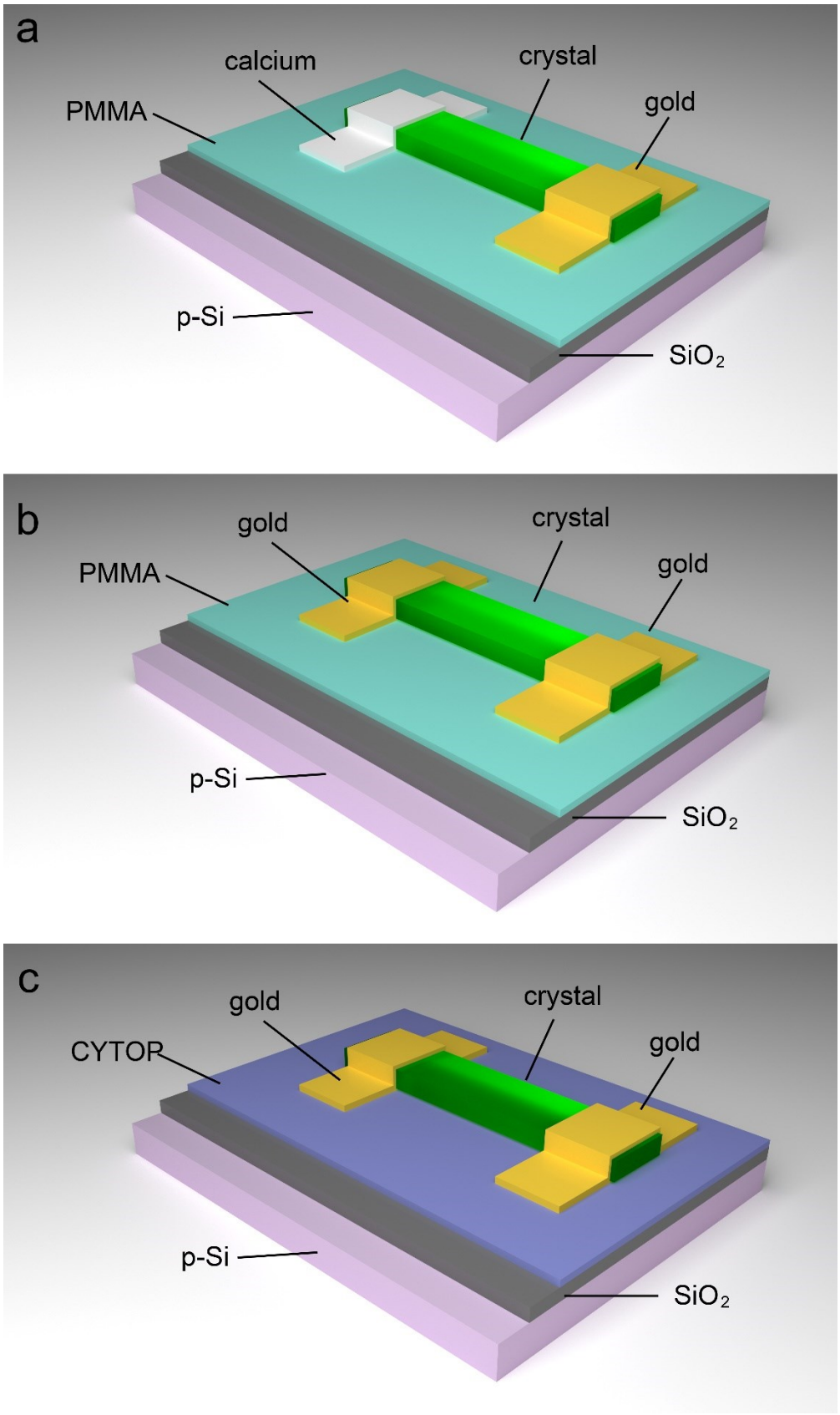

Figure S17. (a) Device structure of asymmetric transistors. (b) Device structure of transistors with symmetric gold electrodes and PMMA buffer layer. (c) Device structure of transistors with symmetric gold electrodes and CYTOP buffer layer.

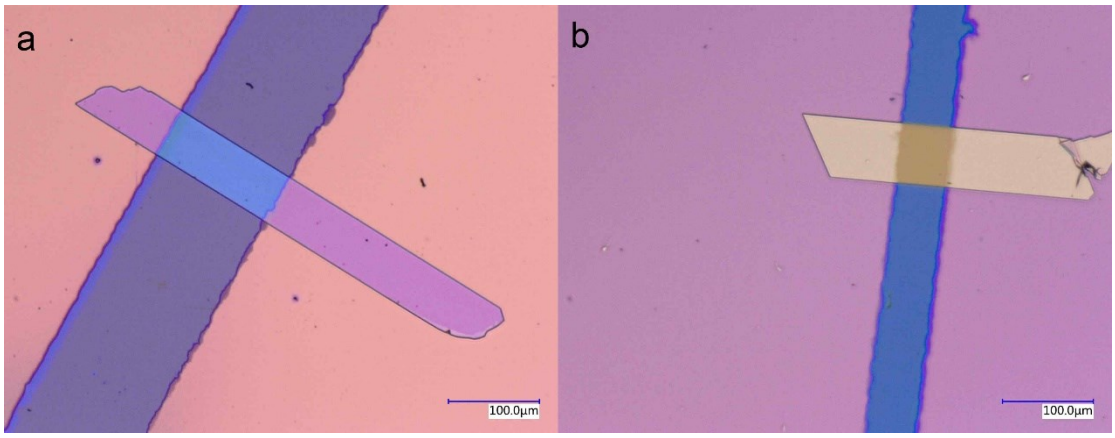

Figure S18. Examples of (a) α-PBTA and (b) β-DBPA lamellar crystals in their corresponding transistors under natural light in microscope.

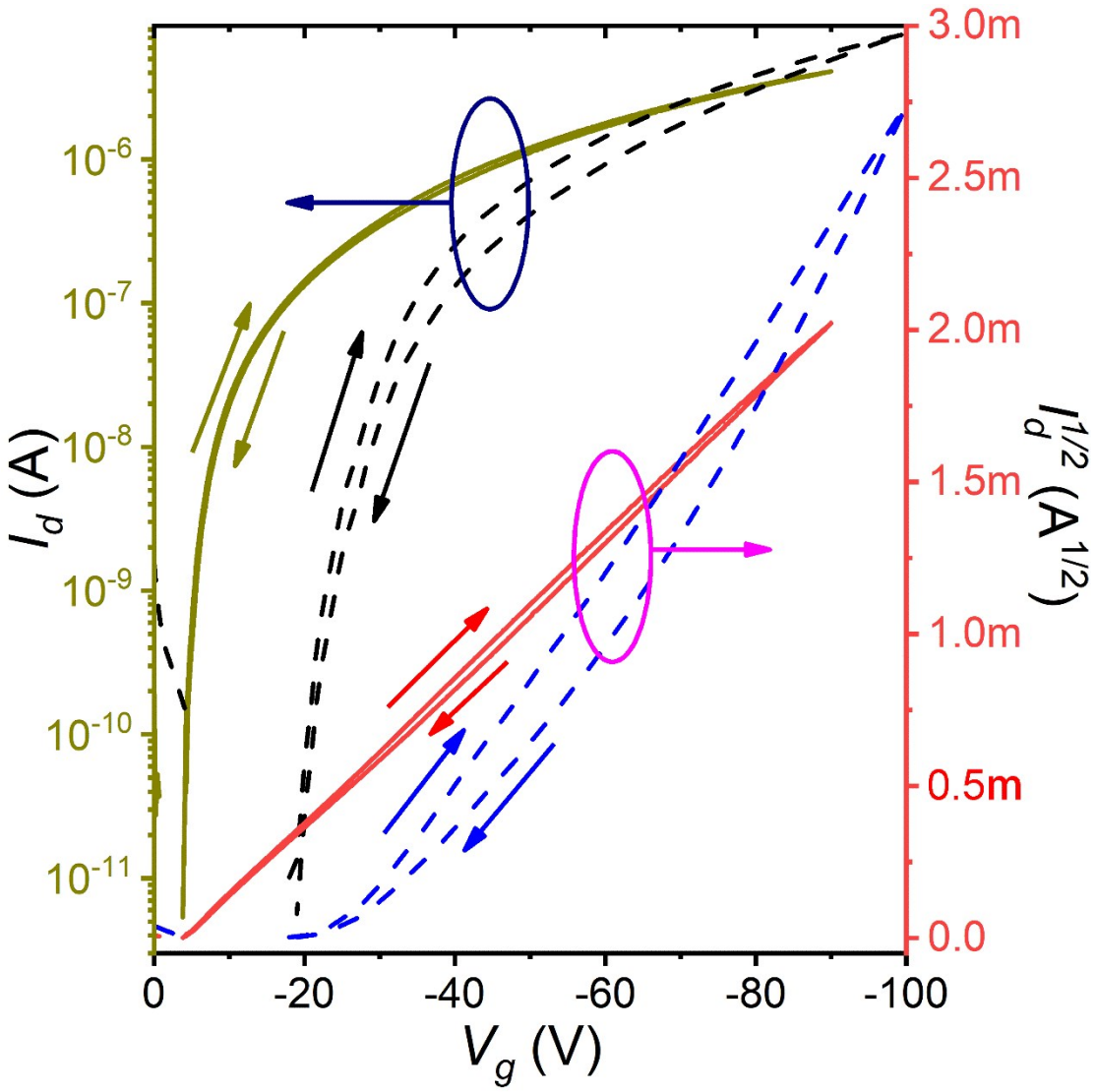

Figure S19. Transfer characteristics of the transistors based on single crystals of α-PBTA. The dash curves were the I-V curves from OFETs with PMMA buffer layer, while the solid curves were the I-V curves from OFETs with CYTOP buffer layer. V_d = -110 and -80 V for OFETs with PMMA and CYTOP buffer layers, respectively. The dark yellow and black lines were corresponded to the $|I_d|$, while the red and blue line were corresponded to $|I_d|^{1/2}$. The transfer curves were swept forward and backward to evaluate their hysteresis.

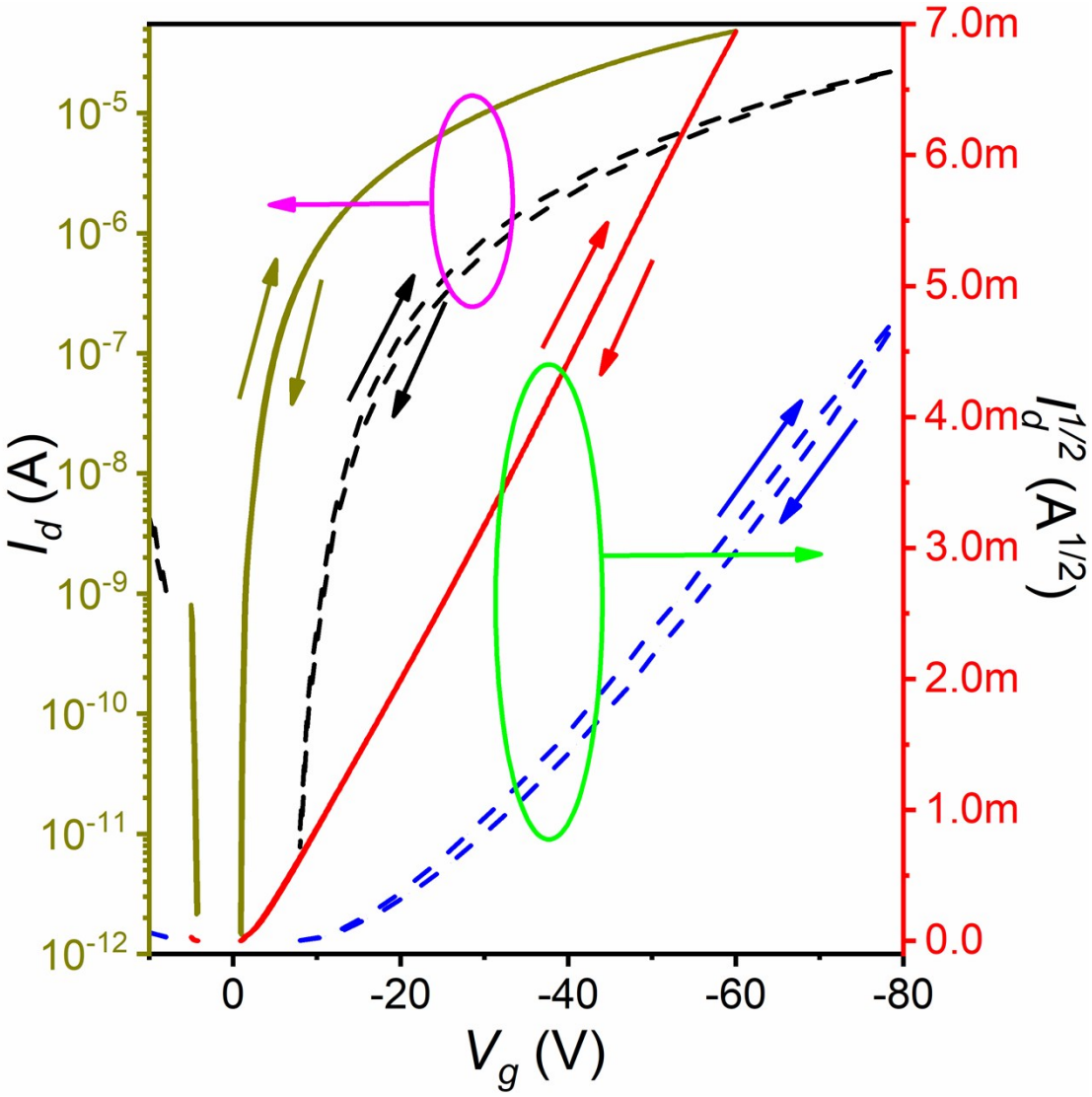

Figure S20. Transfer characteristics of the transistors based on single crystals of β-DBPA. The dash curves were the I-V curves from OFETs with PMMA buffer layer, while the solid curves were the I-V curves from OFETs with CYTOP buffer layer. V_d = -80 and -60 V for OFETs with PMMA and CYTOP buffer layers, respectively. The dark yellow and black lines were corresponded to the $|I_d|$, while the red and blue line were corresponded to $|I_d|^{1/2}$. The transfer curves were swept forward and backward to evaluate their hysteresis.

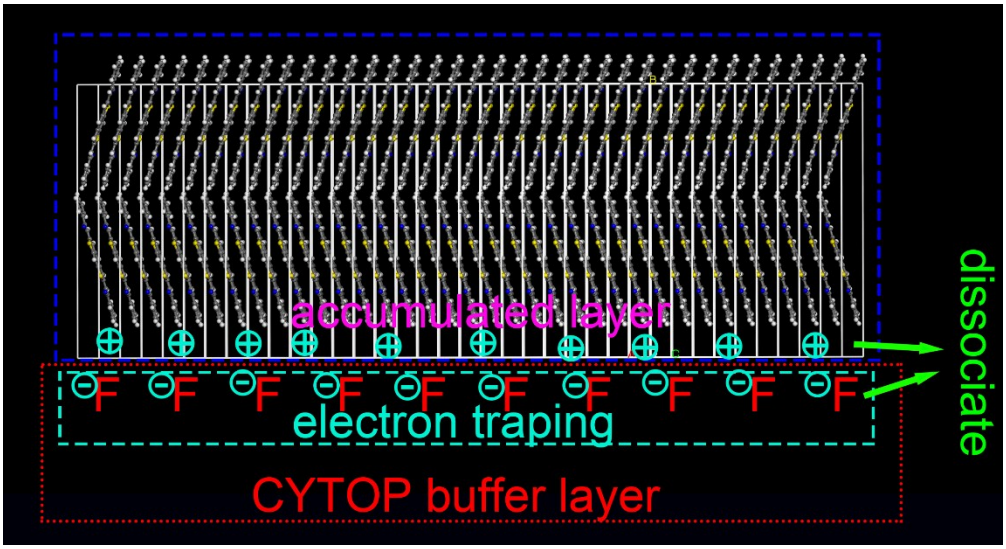

Figure S21. The electric-withdraw F-group acted as electron traps, which promoted the accumulated processes. This processes remarkably reduced the threshold voltage and improved device performance.

The reason of the improvement was the different electric properties on their buffer layer as it was the exclusive difference among them. The highest occupied molecular orbital (HOMO) of the crystal was lower than the work function of gold (Figure S13), resulting in Schottky barrier[S3] in transistors with PMMA. On the other hand, CYTOP had many F-groups with higher electronegativity instead of hydroxymethyl groups in PMMA. As the crystal was attached to the buffer layer, CYTOP caught more electrons from the electron-rich (P-type) OSCs than PMMA did, which resulted in a kind of interfacial doping. The electron plunder processes of CYTOP from semiconductors increased the density of free positive charges and consequently promoted the accumulated processes. Consequently, high-quality organic lamellar crystal and interfacial doping were important for high-performance electronic devices.

Supplementary Tables

Table S1. **The growth conditions of organic crystals**

Compounds	α-PBTA	β-DBPA
sublimation temperature (°C)	240	325
growth temperature (°C)	160	252
flow rate of argon (mL min^{-1})	40	30

Table S2. **Crystallographic data and structural refinement summary for β-DBPA**

	α-PBTA	β-DBPA
crystal system	triclinic	monoclinic
space group	P-1 (2#)	$P2_1$ (14#)
empirical formula	$C_{20}H_{12}N_2S_2$	$C_{28}H_{16}N_2S_2$
molecular weight	344.46	444.55
a (Å)	3.9383(8)	3.9035(4)
b (Å)	5.8698(12)	44.025(6)
c (Å)	18.065(4)	6.0394(6)
α (°)	80.840(3)	90
β (°)	87.250(3)	95.691(8)
γ (°)	86.08(3)	90
V (Å^3)	411.03(8)	1032.7(2)
Z, d_{calcd} (g cm^{-3})	1, 1.392	2, 1.430
diffractometer	CCD	CCD
μ (cm^{-1})	0.326	1.430
radiation type	Mo $K\alpha$	Cu $K\alpha$
radiation wavelength (Å)	0.71073	1.54184
F(000)	178	460.0
goodness of fit	0.957	0.979
temperature (K)	298	287
number of reflections collected/unique	1100/1724	1677/2816
R_{int}	0.0880	0.0684
R_1 ($I > 2.00\sigma(I)$)[a]	0.1151	0.0672
wR_2 ($I > 2.00\sigma(I)$)[b]	0.2446	0.1364
CCDC number	2032334	1936361

[a]$R_1 = \Sigma||F_o|-|F_c||/\Sigma|F_o|$, [b]$wR_2 = [\Sigma w|F_o^2-F_c^2|^2/\Sigma w(F_o^2)^2]^{1/2}$

Table S3. **Photophysical properties of organic crystals**

Compounds	State	PLQY (%)	τ (ns)	K_r ($\times 10^7$ s^{-1})[a]	K_{nr} ($\times 10^7$ s^{-1})[b]
α-PBTA	in CH_2Cl_2	4	1.8 (τ_1 = 0.5) (τ_2 = 5.2)	2.2	53.3
	Crystal	34	3.8	8.9	17.4
β-DBPA	in THF	4	3.0 (τ_1 = 1.5) (τ_2 = 5.0)	1.3	32.0
	Crystal	8	1.1	7.3	83.6

[a]K_r: radiative decay rate, $K_r = \Phi_f/\tau$, where Φ_f and τ referred to the PLQY and fluorescence lifetime, respectively.

[b]K_{nr}: non-radiative decay rate, $K_{nr} = (1-\Phi_f)/\tau$.

Table S4. Comparing of transistors of α-PBTA and β-DBPA with PMMA and CYTOP buffer layers

	α-PBTA		β-DBPA	
	PMMA	CYTOP	PMMA	CYTOP
highest mobility ($cm^2\ V^{-1}\ s^{-1}$)	0.11	0.56	1.71	2.73
maximum on/off ratio	7.38×10^5	7.63×10^5	2.05×10^6	3.32×10^7
channel width (μm)	860	38.0	63.3	80.9
channel length (μm)	50.0	50.0	27.2	55.8
maximum output current (μA)	1.73 @ V_g = -80 V	2.89 @ V_g = -80 V	7.05 @ V_g = -60 V	47.3 @ V_g = -60 V
maximum output current density ($kA\ cm^{-2}$)	0.201 @ V_g = -80 V	7.61 @ V_g = -80 V	11.2 @ V_g = -60 V	58.5 @ V_g = -60 V
maximum hesitate (V)	7.3	0.8	2.5	< 0.1
subthreshold swing (V dec^{-1})	1.5	0.15	0.75	0.10
N_t ($\times10^{11}\ cm^{-2}$)	18.1	1.02	8.69	0.46
V_{th} (V)	-28.77	-5.06	-20.83	-3.60
V_{on} (V)	-18.07	-3.70	-7.83	-1.11
$N_t^{'}$ ($\times10^{11}\ cm^{-2}$)	8.02	0.994	9.74	1.51

Table S5 Optical energy gap and electrochemical energy gap (unit: eV)

Single Crystals	HOMO	LUMO	Electrochemical energy gap	Optical energy gap*
α-PBTA	-3.03	-6.01	2.98	2.70
β-DBPA	-2.90	-5.93	3.03	2.53

* Find out the intercept between tangent line of absorption peak and x-axis first. Then the optical energy gap was calculated by equation $E_g^{opt} = hc/\lambda_{intercept}$

Table S6. Subthreshold Swing and Interfacial trap density in inorganic FETs (in 2020) and OFETs

	Subthreshold Swing (V dec^{-1})	Interfacial trap density (× 10^{12} cm^{-2})	Ref
AlGaN/GaN	0.1416	18.0	S4
MoS2 on ZrO2	0.143	--	S5
F-doping In-O thin-films	1.87	--	S6
polycrystalline-silicon tunnel transistor	0.023	--	S7
In–Ga–Zn–O	0.131	0.890	S8
amorphous InZnSnO	0.12	--	S9
Si0.87Ge0.13	--	0.1	S10
C_8-BTBT/SiO_2	0.480	2.90	S11
C_8-BTBT/HfO_2	0.145	5.12	
selective buried oxide (SELBOX) TFET with δp+ SiGe layer	0.045	0.10	S12
dinaphtho[2,3-b:2',3'-f]thieno[3,2-b]thiophene	0.079	--	S13
CdS thin film	0.25	0.16	S14
AlGaN/GaN	0.085	1.1×10^{-3}	S15
InAlN/GaN	0.085	0.468	S16
ZnO bilayer thin film	0.21	0.372	S17
IGO	0.096	0.589	S18
Si/SiGe tunnel transistor	0.032	--	S19
MoS2	0.097	1.66	S20
InGaZnO Thin-Film	0.8	--	S21
ZnSnO	0.13	0.6	S22

Crystallographic Datas

Crystallographic Data S1.

Crystallographic information file (CIF) of the α-PBTA.

Crystallographic Data S2.

Crystallographic information file (CIF) of the β-DBPA.

Supplementary reference

S1. J. K. Jeong, J. H. Jeong, H. W. Yang, J.-S. Park, Y.-G. Mo and H. D. Kim, *Appl. Phys. Lett.*, 2007, **91**, 113505.

S2. K. P. Pernstich, S. Haas, D. Oberhoff, C. Goldmann, D. J. Gundlach, B. Batlogg, A. N. Rashid and G. Schitter, *J. Appl. Phys.*, 2004, **96**, 6431-6438.

S3. G. Horowitz, *Adv. Mater.*, 1998, **10**, 365-377.

S4. H. Zhang, G. J. Chen, J. C. Zhang, X. F. Zheng, H. Zhou, S. L. Zhao and Y. Hao, *J. Supercrit. Fluids*, 2020, **158**, 104746.

S5. X. J. Song, J. P. Xu, L. Liu, Y. H. Deng, P. T. Lai and W. M. Tang, *Nanotechnology*, 2020, **31**, 135206.

S6. A. Sil, L. Avazpour, E. A. Goldfine, Q. Ma, W. Huang, B. H. Wang, M. J. Bedzyk, J. E. Medvedeva, A. Facchetti and T. J. Marks, *Chem. Mater.*, 2020, **32**, 805-820.

S7. W. C. Y. Ma, M. J. Li, S. M. Luo, J. H. Lin and C. J. Tsai, *Thin Solid Films*, 2020, **697**, 137818.

S8. H. J. Li, D. D. Han, J. C. Dong, Z. Yi, X. B. Zhou, S. D. Zhang, X. Zhang and Y. Wang, *IEEE Trans. Electron Devices*, 2020, **67**, 518-523.

S9. A. D. Lestari, M. Putri, Y. W. Heo and H. Y. Lee, *J. Nanosci. Nanotechno.*, 2020, **20**, 252-256.

S10. H. W. Lee, Y. Choi, D. Shin, D. S. Byeon and D. H. Ko, *Thin Solid Films*, 2020, **707**, 138048.

S11. S. Jiang, Q. Wang, J. Qian, J. Guo, Y. Duan, H. Wang, Y. Shi and Y. Li, *Acs Appl. Mater. Inter.*, 2020, **12**, 26267-26275.

S12. P. Ghosh, A. Roy and B. Bhowmick, *Appl. Phys. a-Mater.*, 2020, **126**, 330.

S13. M. Geiger, R. Acharya, E. Reutter, T. Ferschke, U. Zschieschang, J. Weis, J. Pflaum, H. Klauk and R. T. Weitz, *Adv. Mater. Interfaces*, 2020, **7**, 1902145.

S14. M. S. De Urquijo-Ventura, M. G. S. Rao, S. Meraz-Davila, J. A. Torres-Ochoa, M. A. Quevedo-Lopez and R. Ramirez-Bon, *Polymer*, 2020, **191**, 122261.

S15. X. Cui, W. J. Cheng, Q. L. Hua, R. R. Liang, W. G. Hu and Z. L. Wang, *Nano Energy*, 2020, **68**, 104361.

S16. P. Cui, J. Zhang, M. Jia, G. Y. Lin, L. C. Wei, H. C. Zhao, L. Gundlach and Y. P. Zeng, *Jpn. J. Appl. Phys.*, 2020, **59**, 020901.

S17. X. Chen, J. X. Wan, H. Wu and C. Liu, *Acta Mater.*, 2020, **185**, 204-210.

S18. K. Y. Chen, C. C. Yang, C. Y. Huang and Y. K. Su, *Rsc Adv.*, 2020, **10**, 9902-9906.

S19. T. Bentrcia, F. Djeffal, F. Hichem and Z. Dibi, *Silicon-Neth*, 2020, **12**, 945-953.

S20. J. Y. Zou, L. S. Wang and F. X. Chen, *Aip Adv.*, 2019, **9**, 095061.

S21. Y. Zhang, H. T. Xie and C. Y. Dong, *Micromachines-Basel*, 2019, **10**, 779.

S22. J. Q. Zhang, J. G. Lu, Y. D. Lu, S. L. Yue, R. K. Lu, X. F. Li, J. H. Zhang and Z. Z. Ye, *Appl. Phys. a-Mater.*, 2019, **125**, 362.